

Numerical simulation of dynamic development of keyhole in double-sided arc welding

C S Wu^{1,3}, J S Sun¹ and Y M Zhang²

¹ MOE Key Lab for Liquid Structure and Heredity of Materials, Institute for Materials Joining, Shandong University, 73 Jingshi Road, Jinan 250061, People's Republic of China

² Center for Manufacturing and Department of Electrical and Computer Engineering, College of Engineering, University of Kentucky, Lexington, Kentucky 40506, USA

E-mail: wucs@sdu.edu.cn

Received 18 September 2003

Published 25 February 2004

Online at stacks.iop.org/MSMSE/12/423 (DOI: 10.1088/0965-0393/12/3/005)

Abstract

Double-sided arc welding (DSAW) is a novel process for joining metals that is capable of achieving deep narrow penetration in a single pass with minimized distortion. A clear understanding of the process fundamentals is critical in order to fully examine the potential of DSAW, to guide the further developments of the process, to direct the practicability study, and to design the process parameters. This paper aims at developing a numerical model for examining and simulating the dynamic keyhole establishment process, which will be a key in developing an effective control technology for DSAW. The model is used to determine the geometrical shape of the keyhole and the weld pool, and the temperature distribution in the workpiece. Quantitative information on the establishment of the keyhole in DSAW, such as the transient development of the keyhole and the weld pool, the increase rate of the depth of the surface depression, the time interval from full penetration to the keyhole establishment, the minimum span of the weld pool for describing the conditions required to complete the keyhole establishment, and variation of the overflow height of the weld pool surface on the plasma arc welding side, has been obtained through numerical analysis. The DSAW experiments show that the predicted weld cross-section is in agreement with the measured one. The results lay a foundation for guiding the further development of the DSAW process and its effective control.

Nomenclature

c_p	specific heat, $\text{J kg}^{-1} \text{K}^{-1}$
g	acceleration due to gravity, 9.8 m s^{-2}
H	workpiece thickness, m
$\vec{i}, \vec{j}, \vec{k}$	unit vector of coordinates

³ Author to whom any correspondence should be addressed.

I	welding current, A
J	current density flux, $A\ m^{-2}$
K	thermal conductivity, $W\ m^{-1}\ K^{-1}$
n	vector normal to the surface
\vec{n}_b	unit vector normal to the surface
P_p	arc pressure of PAW, Pa
P_g	arc pressure of GTAW, Pa
q_{gq}	heat flux density of GTAW, $W\ m^{-2}$
q_{pq}	heat flux density of PAW, $W\ m^{-2}$
r_0	radius of PAW orifice, m
r_{jp}	distribution radius of PAW current, m
r_{jg}	distribution radius of GTAW current, m
$r = \sqrt{x^2 + y^2}$	
T	temperature, K
t	time, s
T_m	melting point, 1773 K
T_0	ambient temperature, K
u_0	welding speed, $m\ s^{-1}$
U_p	arc voltage of PAW, V
U_g	arc voltage of GTAW, V
x, y, z	coordinates, m
z^*	transformed z -coordinate
α	heat loss coefficient, $W\ m^{-2}\ K^{-1}$
ρ	density, $kg\ m^{-3}$
γ	surface tension coefficient, $1.0\ N\ m^{-1}$
σ	electrical conductivity, $\Omega^{-1}\ m^{-1}$
σ_q	arc heat flux distribution parameter of PAW, m
σ_{gq}	arc heat flux distribution parameter of GTAW, m
$\lambda, \lambda_p, \lambda_g$	Lagrangian multiplier
Ψ	configuration function of weld pool surface
Φ	electric potential
n_p	arc power efficiency of PAW
n_g	arc power efficiency of GTAW
$\Psi_x = \partial\Psi/\partial x$	
$\Psi_y = \partial\Psi/\partial y$	
$\Psi_{xy} = \partial^2\Psi/\partial x\partial y$	
$\Psi_{xx} = \partial^2\Psi/\partial^2 x$	
$\Psi_{yy} = \partial^2\Psi/\partial^2 y$	

1. Introduction

Double-sided arc welding (DSAW) is a new arc welding process invented and developed at the University of Kentucky [1–3]. The DSAW system uses two torches on the opposite sides of the workpiece to force the welding current to flow through the thickness of the workpiece disconnected from the power supply (figure 1(b)). Through-thickness direction of the welding current and establishment of a keyhole both help enhance the concentration of the arc and the

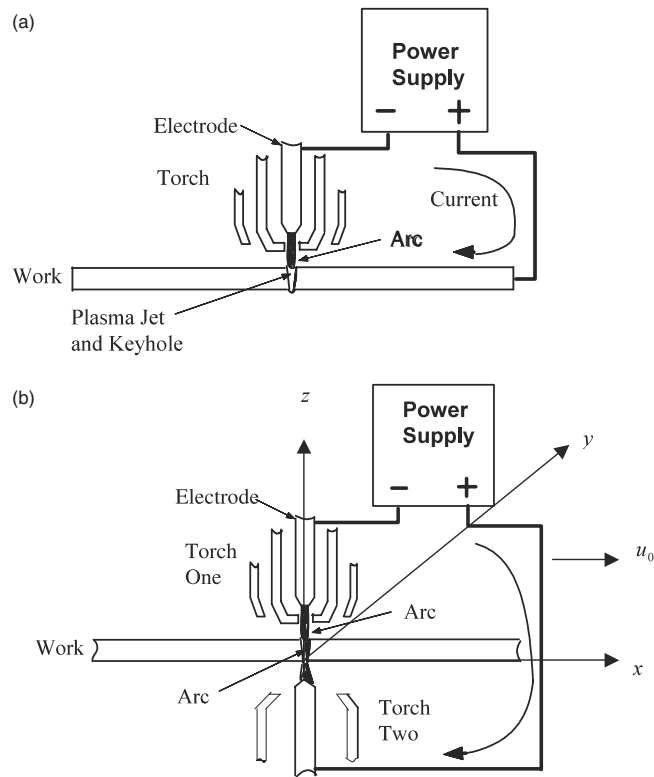


Figure 1. Schematics of PAW and DSAW. (a) Regular welding system; (b) DSAW system and coordinate system.

density of the arc energy. The uniqueness of DSAW lies in its strong penetration capability and its symmetric hour-glass-shaped welds. A shipyard's preliminary study indicated that this process has potential use for minimizing distortion while at the same time improving throughput when making butt welds [4]. If shown to be of practical value to the shipbuilding industry, a process could result that would be cheaper to implement and have greater versatility than the laser welding process which is being investigated for ship construction with distortion reduction as a primary goal.

As can be seen in figure 1(a), a regular plasma arc welding (PAW) system uses an electrical connection (ground cable) between the workpiece and power supply to allow the welding current to complete the loop. The electric arc is established between the workpiece and the torch. In a DSAW system, the workpiece is disconnected from the power supply and a second gas tungsten arc welding (GTAW) torch is placed on the opposite side of the workpiece to complete the current loop (figure 1(b)). As a result, electric arcs are simultaneously established between the workpiece and each of the two torches. It is found that this configuration has greatly improved the penetration capability. For example, stainless steel plates up to 12.7 mm ($\frac{1}{2}$ inch) thick can be welded in a single pass without bevels under the condition of welding current 70 A [2]. Although the GTAW electrode has positive polarity in DSAW, the electrode is not overheated because the welding current is much lower. For the voltage behaviour when a through keyhole is achieved, experiments show that the voltage decrease from nonkeyhole to keyhole mode is approximately 3.5 V [2]. Unlike in conventional arc welding where the potential of the workpiece is fixed, the potential of the workpiece in DSAW is floating.

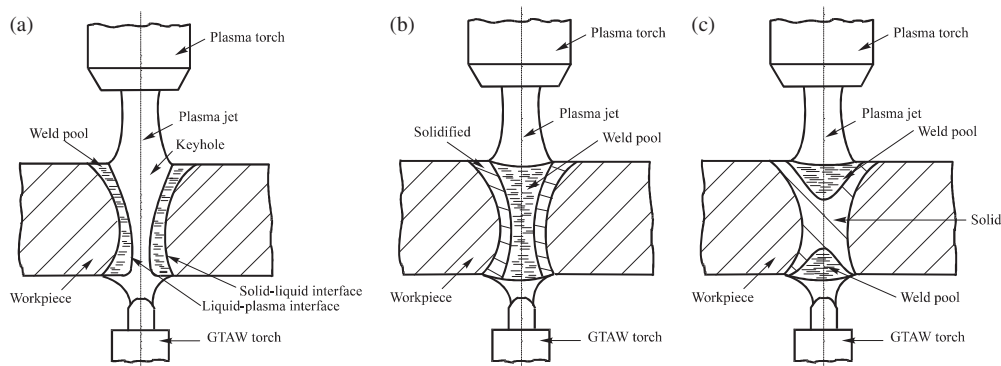


Figure 2. Weld pool transition after current decrease. (a) Transient state 1—keyhole; (b) transient state 2—complete weld pools; (c) incomplete weld pools.

The voltages of the arcs on both sides of the workpiece will thus vary when the location of the workpiece in relation to the electrodes fluctuates or changes. To assure a symmetrical heat input, which is desired for minimizing the distortion, the distances from each of the electrodes to the workpiece should be maintained at pre-specified desirable levels.

Although DSAW is capable of penetrating 12.7 mm ($\frac{1}{2}$ inch) thick steels in a single pass [2, 3], unlike laser welding where the keyhole is primarily established by the vaporization of the metal, the vaporization in DSAW is much reduced and the keyhole is primarily established by the force of the high speed plasma jet on the molten metal. The resultant weld pool is larger or wider than that in laser welding.

To develop an effective method to dynamically minimize the weld pool, the possibility of establishing a pulsed keyhole has been analysed [2, 3]. If the heat input and the plasma pressure are assumed sufficient, then the depth of the non-penetrated keyhole created by the plasma pressure will increase rapidly such that the penetrated keyhole mode will be quickly established. Hence, if the welding current is large enough to provide a sufficient plasma pressure, which is proportional to the square of the current [5], and heat input, the penetrated keyhole mode may be established at a minimized average width of the weld pool. If the current is then quickly decreased to a low level, which cannot provide a sufficient heat input and plasma pressure to maintain a penetrated keyhole, the keyhole will close quickly and the molten pool will shrink as illustrated in figure 2. In this way, the weld metal can be prevented from being blown away from the workpiece. Hence, the penetrated keyhole can be periodically established and then closed to maintain the process at a dynamically stable mode which guarantees full penetration with minimized heat input. The resultant operating mode has been termed controlled pulse keyhole.

It can be seen that controlled pulse keyhole could be an effective mode to conduct DSAW of thick materials. However, despite the progress in process, system, and applications, there is a lack of understanding of the process fundamentals. To design an effective control system, the dynamic keyhole establishment process must be understood and be used to design the amplitude of the peak current so that the keyhole is established at a minimal width of the weld pool. To this end, a numerical model is needed to analyse the behaviours of the developing keyhole and weld pool during the keyhole establishment process.

It should be pointed out that modelling has proved an effective method to gain insight into welding processes through the exploratory work during the 1980s by Oreper [6, 7], Kou [8], Lin [9], Zacharia [10], Pardo [11], Tekriwal [12], their co-workers, and many other researchers. The authors have also developed a model for determining gas metal arc (GMA) weld pool

behaviours, which deals with the arc heat flux distribution at the deformed pool surface, the heat content of the filler droplets within the weld pool and the droplets' impact on the pool surface [13, 14]. However, no studies have been done to model DSAW weld pool behaviours although the early exploratory work has established necessary foundations. In this study, a numerical model is developed for quantitatively analysing the dynamic behaviours of keyhole in DSAW.

2. Mathematical model

The following simplifications are introduced, either to make the simulation computationally practicable or due to insufficient information concerning a particular aspect of the problem. (1) As a first step, the fluid flow inside the weld pool is not considered. (2) The current density on both the front (PAW side) and the back (GTAW side) surfaces is distributed in Gaussian form, but with different distribution parameters. (3) The heat flux on both the front (PAW side) and the back (GTAW side) surfaces is distributed in Gaussian form, but with different distribution parameters. (4) Consistent with the low heats of fusion which characterize most metals, latent heat effects are neglected [15]. (5) All thermophysical properties are assumed constant and are representative of AISI 304 stainless steel.

Figure 1(b) is a schematic of the DSAW process where the workpiece is welded at the flat position. The PAW and GTAW torches move simultaneously at a constant speed u_0 during welding along the x -axis direction. The coordinate system $o-xyz$ is attached to the torch system. In particular, assume that the axes of the tungsten electrodes of the two torches are aligned and are referred to as the electrode axis. Also assume that the workpiece is flat with the electrode axis as the normal. Then the electrode axis and the bottom surface (plane) define the z -axis and the x - y plane, respectively. The intersection of the axis and the plane is thus the origin of the coordinate system. Figure 1(b) shows the defined $o-xyz$ coordinate system.

2.1. Current density

The current from the GTAW electrode to the PAW electrode flows along two paths in DSAW. Before the keyhole is established, the current flows into the workpiece through the GTAW side's surface, then travels through the workpiece along the thickness, and finally flows out of the workpiece from the PAW side's surface. Because the weld pool surface on both sides is deformed by the arc pressure even prior to the establishment of the keyhole, the current could flow into and out of the workpiece at different locations on the surface. After the keyhole is established, part of the current may directly flow through the keyhole from the GTAW electrode to the PAW electrode without going through the workpiece. In this case, the arc will exist along the entire keyhole. However, in regular PAW, the current does not flow through the keyhole [16]. As a result, DSAW has a unique heat generation/compensation mechanism along the keyhole or the thickness direction of the workpiece [2]. This heat generation/compensation mechanism helps the DSAW achieve deeper penetration and a narrower weld. Therefore, the determination of the current distribution plays a critical role in studying the DSAW process.

The current density distribution is governed by the steady-state Maxwell equation [17]:

$$\nabla \cdot \vec{J} = 0. \quad (1)$$

Ohm's law gives the following relationship [16]:

$$\vec{J} = -\sigma \left(\frac{\partial \Phi}{\partial x} \vec{i} + \frac{\partial \Phi}{\partial y} \vec{j} + \frac{\partial \Phi}{\partial z} \vec{k} \right). \quad (2)$$

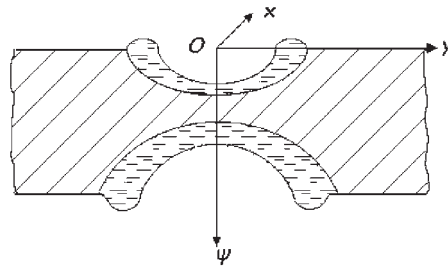


Figure 3. Schematic of transverse cross-section prior to formation of keyhole (upper side, PAW; lower side, GTAW).

The Maxwell equation's Laplace form, i.e. the current continuity equation, is obtained by substituting (2) in (1):

$$\frac{\partial^2 \Phi}{\partial x^2} + \frac{\partial^2 \Phi}{\partial y^2} + \frac{\partial^2 \Phi}{\partial z^2} = 0. \quad (3)$$

The boundary condition of the control equation (3) is

on the PAW side surface:

$$\frac{\partial \Phi}{\partial n} = -\frac{1}{\sigma} \frac{I}{\pi r_{jp}^2} \exp\left(-\frac{r^2}{r_{jp}^2}\right) \quad (4a)$$

on the GTAW side surface:

$$\frac{\partial \Phi}{\partial n} = \frac{1}{\sigma} \frac{I}{\pi r_{jg}^2} \exp\left(-\frac{r^2}{r_{jg}^2}\right) \quad (4b)$$

on the surface:

$$\frac{\partial \Phi}{\partial n} = 0 \quad (4c)$$

where n is the normal vector of the workpiece surface, r_{jp} is the distribution radius of the current at the surface on the PAW side, r_{jg} is the distribution radius of the current at the surface on the GTAW side, $r = \sqrt{x^2 + y^2}$. For PAW, $r_{jp} = (1.3-1.4)r_0$ [18] where r_0 is the orifice radius and is 0.785 mm in this study. r_{jg} is selected based on experimental data [19], and it takes a value of 1.25 mm in this research.

Equations (1)–(3) correspond to the metal in the workpiece. The current density distribution \vec{J} can be obtained by solving (2)–(4).

2.2. Deformation equation

Figure 3 shows the transverse cross-section along the weld seam prior to the establishment of the keyhole. As can be seen, the weld pool surface is deformed by the arc pressure and cavities are formed. Overflow of the weld pool surface occurs and slight reinforcement is present on both sides of the solidified weldment behind the arc, i.e. $x < 0$. Such slight reinforcement continues until the growth of the volume of the cavities stops. Because no filler materials are used, the slight reinforcement results from the melted metal near the arc centreline where the pool surface is depressed. The equations that

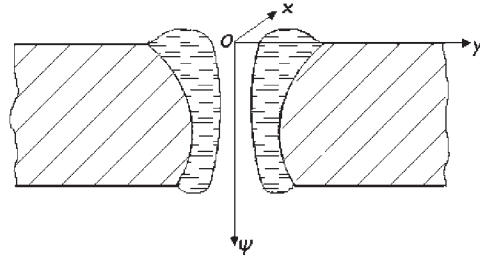


Figure 4. Schematic of transverse cross-section after keyhole is established (upper side, PAW; lower side, GTAW).

control the deformation of the weld pool surface can be derived from the calculus of variations [20]:

on the PAW torch side:

$$P_p - \rho g \Psi + \lambda_p = -\gamma \frac{(1 + \Psi_y^2) \Psi_{xx} - 2 \Psi_x \Psi_y \Psi_{xy} + (1 + \Psi_x^2) \Psi_{yy}}{(1 + \Psi_x^2 + \Psi_y^2)^{3/2}} \quad (5)$$

on the GTAW torch side:

$$-P_g + \rho g (\Psi - H) + \lambda_g = -\gamma \frac{(1 + \Psi_y^2) \Psi_{xx} - 2 \Psi_x \Psi_y \Psi_{xy} + (1 + \Psi_x^2) \Psi_{yy}}{(1 + \Psi_x^2 + \Psi_y^2)^{3/2}}. \quad (6)$$

The arc pressure is current density dependent and can be determined by $\mu_0 I J / 4\pi$ [20], J can be obtained by solving the Maxwell's equation. In equations (5) and (6), λ_p and λ_g are Lagrangian multipliers resulting from derivation based on the calculus of variation [20], and their physical meanings are the sum of other forces acting on the pool surface save the arc pressure, hydrostatic forces and surface tension.

After the full penetration or keyhole is established, depression and reinforcement form on the solidified weldment on the PAW side and GTAW side, respectively. Figure 4 gives the transverse cross-section along the weld seam after the keyhole is established. The shape of the weld pool, including the keyhole, is governed by the following control equation

$$P_p - P_g - \rho g \Psi + \lambda = -\gamma \frac{(1 + \Psi_y^2) \Psi_{xx} - 2 \Psi_x \Psi_y \Psi_{xy} + (1 + \Psi_x^2) \Psi_{yy}}{(1 + \Psi_x^2 + \Psi_y^2)^{3/2}}. \quad (7)$$

The boundary conditions for control equations (5)–(7) are

$$\begin{aligned} \text{on the upper surface of workpiece,} \quad & \Psi(x, y) = 0, \quad T \leq T_m \\ \text{on the bottom surface of workpiece,} \quad & \Psi(x, y) = H, \quad T \leq T_m. \end{aligned}$$

2.3. Energy equation

After the keyhole is established, the weld pool surface is severely deformed on both sides. The description of the boundary condition on the deformed pool surface becomes inconvenient in the Cartesian coordinate system. To overcome this inconvenience, the non-orthogonal surface-fitted coordinate system $o-xyz^*$ is used [21]. Consider the following coordinate transform:

$$x = x, \quad y = y, \quad z^* = \frac{z - B(x, y)}{F(x, y) - B(x, y)} \quad (8)$$

where $F(x, y) = \Psi(x, y)$ and $B(x, y) = \Psi(x, y) - H$ are the front and back surfaces, respectively. That is,

$$z^* = \frac{z - \Psi(x, y) + H}{H}.$$

On the front surface, $z^* = 1$ due to $z = \Psi(x, y)$. On the back surface, $z^* = 0$ due to $z = \Psi(x, y) - H$.

The energy equations in (x, y, z) coordinates and (x, y, z^*) coordinates are given in (9) and (10), respectively

$$\rho c_p \left(\frac{\partial T}{\partial t} - u_0 \frac{\partial T}{\partial x} \right) = \frac{\partial}{\partial x} \left(K \frac{\partial T}{\partial x} \right) + \frac{\partial}{\partial y} \left(K \frac{\partial T}{\partial y} \right) + \frac{\partial}{\partial z} \left(K \frac{\partial T}{\partial z} \right) \quad (9)$$

$$\rho c_p \left(\frac{\partial T}{\partial t} - u_0 \frac{\partial T}{\partial x} \right) = \frac{\partial}{\partial x} \left(K \frac{\partial T}{\partial x} \right) + \frac{\partial}{\partial y} \left(K \frac{\partial T}{\partial y} \right) + S \frac{\partial}{\partial z^*} \left(K \frac{\partial T}{\partial z^*} \right) + C_t K \quad (10)$$

where

$$C_t = 2 \left(\frac{\partial z^*}{\partial x} \cdot \frac{\partial^2 T}{\partial x \partial z^*} + \frac{\partial z^*}{\partial y} \cdot \frac{\partial^2 T}{\partial y \partial z^*} \right) \quad \text{and} \quad S = \left(\frac{\partial z^*}{\partial x} \right)^2 + \left(\frac{\partial z^*}{\partial y} \right)^2 + \left(\frac{\partial z^*}{\partial z} \right)^2.$$

The boundary conditions are as follows.

Front surface:

$$-K \cdot \nabla T \cdot \vec{n}_b = q_{pq} \quad (11)$$

$$q_{pq} = \frac{\eta_p I U_p}{2\sigma_{pq}^2} \exp\left(-\frac{r^2}{2\sigma_{pq}^2}\right). \quad (12)$$

Back surface:

$$-K \cdot \nabla T \cdot \vec{n}_b = q_{gq} \quad (13)$$

$$q_{gq} = \frac{\eta_T I U_g}{2\sigma_{gq}^2} \exp\left(-\frac{r^2}{2\sigma_{gq}^2}\right). \quad (14)$$

On all other surfaces:

$$K \cdot \nabla T = \alpha(T - T_0) \quad (15)$$

where σ_{pq} and σ_{gq} are determined based on experimental measurements [19]. The determination of the combined heat transfer coefficient α for radiative and convective boundary conditions is discussed in [22]. Equation (15) describes the heat loss on the surfaces of the workpiece. The left-hand side is the heat flow conducted to the surface from inside the workpiece, the right-hand side is the heat flow dissipated from the surface due to radiation and convection, and both terms should be equal.

3. Numerical solution

The thermal property parameters K , c_p , α are temperature dependent and their values are referred to [22, 23]. Other thermal property parameters used in calculation are shown in table 2. The flow chart of the numerical program is given in figure 5.

In the computation, the thickness, width, and length of the workpiece are 9.5 mm, 80 mm, and 150 mm, respectively. Table 1 lists all the welding parameters used in the computation.

The thermal property parameters used in the calculation are shown in table 2. Because the fluid flow in the weld pool is not considered in this study, the surface tension coefficient γ is

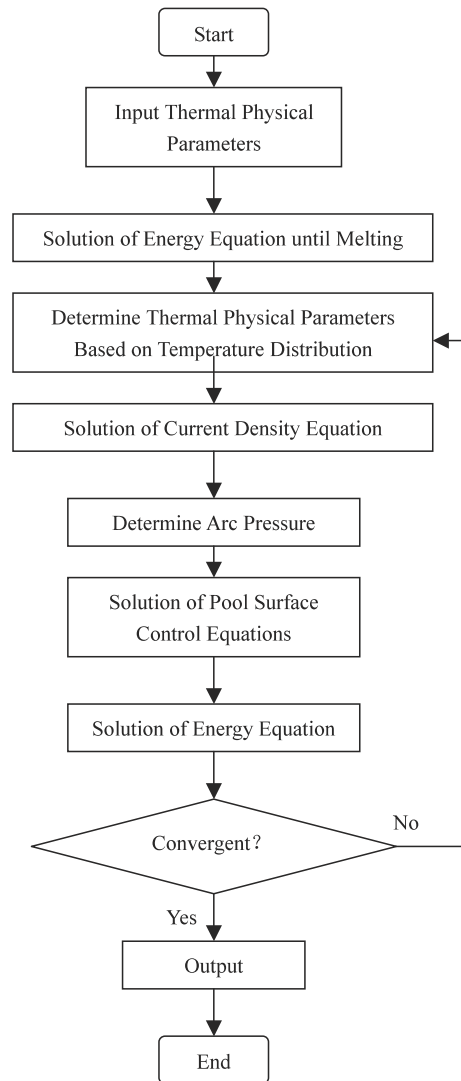


Figure 5. Flow chart of the numerical analysis program.

Table 1. Welding parameters.

Current	67 A
Speed	1.3 mm s^{-1}
Voltage	45 V
PAW stand-off distance	6 mm
GTAW arc length	10 mm

taken as a constant. In this study, 1.0 N m^{-1} [14, 23] is used as the surface tension coefficient for stainless steel.

The current flows through both the workpiece and the keyhole. During numerical solution, the current distribution in the workpiece and in the arc is computed as the arc-workpiece system which is governed by the Maxwell's equation. The electrical conductivity

Table 2. Thermal property parameters of stainless steel.

ρ (kg m ⁻³)	T_m (K)	γ (N m ⁻¹)	μ_m
7.2×10^{-3}	1732	1	1.66×10^{-6}

σ is $1.4 \times 10^6 \Omega^{-1} \text{m}^{-1}$ for stainless steel [24] and $7.49 \times 10^3 \Omega^{-1} \text{m}^{-1}$ for plasma [25], corresponding to a plasma temperature of 15 000 K and argon gas of 1 atm pressure.

4. Results and discussion

Figures 6 and 7 illustrate the results of computation on the dynamic process of keyhole formation in longitudinal and transverse directions. The abscissa of $x = 0$ indicates the origin of the moving torch coordinate and the arc axis. It can be seen that full penetration and the fully penetrated keyhole, for the given current (67 A), welding speed (1.3 mm s^{-1}), and workpiece (9.5 mm thick stainless steel), are established in approximately 1.35 and 1.65 s after the arc is ignited. As can be observed in the figures, when full penetration is established, the sum of the depths of the partial cavities on the two sides of the workpiece is only approximately 3 mm, less than one-third of the workpiece thickness. The remaining 6.5 mm (more than two-thirds) of the workpiece thickness is rapidly penetrated in only approximately 0.3 s to establish the fully penetrated keyhole. It appears that the establishment of full penetration accelerates the establishment of the keyhole.

The dynamic development process of the weld pool and keyhole geometrical parameters after the arc is ignited can also be obtained from the computation used to produce figures 6 and 7. Figure 8 illustrates the development of the partial-keyhole (cavity) depth on both the GTAW and PAW side. As can be observed in figure 8, before full penetration is established, the cavity depths on both sides of the workpiece increase at approximately constant rates, i.e. 0.37 mm s^{-1} for the GTAW side and 1.9 mm s^{-1} for the PAW side. However, after full penetration is established, the rates increase rapidly.

Define the depth of the partial keyhole as the sum of the depths of the cavities on the GTAW side and PAW side. The increase of the depth of the partial keyhole from zero to the full thickness of the plate, i.e. 9.5 mm in this study, can be used to better demonstrate the development process of the keyhole. Figure 9 depicts the development process of the keyhole using the depth of the partial keyhole. It can be seen that during the first 1.5 s, the depth of the partial keyhole only increases 3.66 mm, less than 40% of the thickness. The increase rate is less than 2.5 mm s^{-1} . However, in the last 0.15 s, the depth increases 5.84 mm. That is, the keyhole establishment process, as described by the increase of the depth of the partial keyhole, is finished primarily in a very short period of time at a very high speed, approximately 40 mm s^{-1} .

Figure 9 shows that before full penetration is established, the average increase rate of the depth of the partial keyhole is 2.3 mm s^{-1} (3.05 mm per 1.35 s). After full penetration is established, the average increase rate becomes 21.5 mm s^{-1} , i.e. 9.5 mm at 1.65 s minus 3.05 mm at 1.35 s divided by the 0.3 s time interval. However, the increase rate of the depth is not constant after full penetration is established. In the first 0.15 s, the increase rate of the depth is 4 mm s^{-1} . This rate is slightly higher than the average rate before full penetration is established. However, it is only approximately one-tenth of the rate in the last 0.15 s which is 40 mm s^{-1} . This suggests that the last 0.15 s in this study is a very specific period.

To analyse the phenomenon observed above, let us examine figure 6 which demonstrates the development of the geometry of the weld pool in the longitudinal direction. Denote $(z, x_{mf}(z))$ as a point on the front solid-liquid interface and $(z, x_{mr}(z))$ as a point on the rear

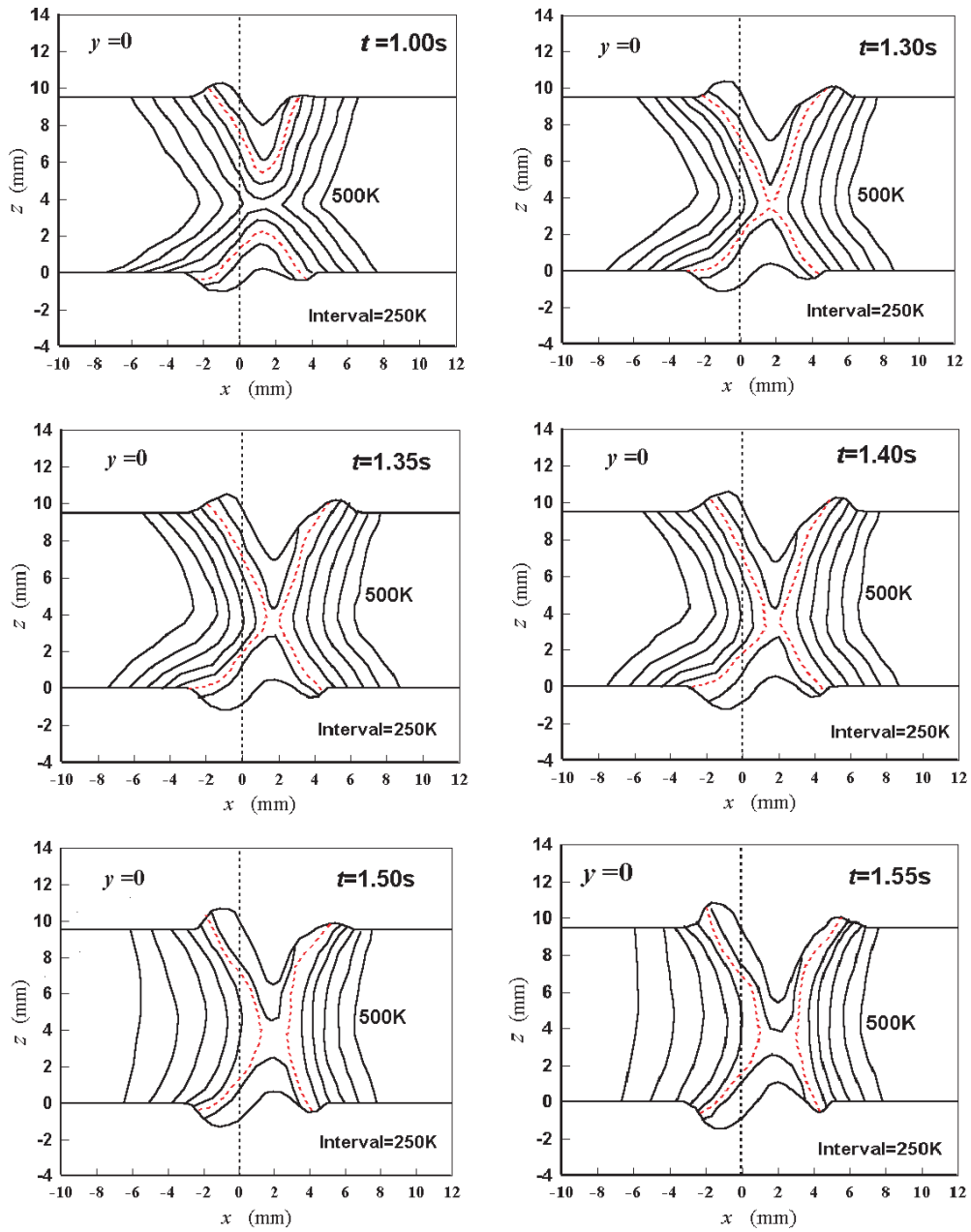


Figure 6. Dynamic development of longitudinal temperature field. The vertical dotted line at $x = 0$ indicates the location where the arc was ignited. —, isothermal; ·····, solid–liquid boundary.

solid–liquid interface (figure 10(a)). Then $s(z) = x_{mf}(z) - x_{mr}(z)$ defines the span of the weld pool at z (figure 10(b)). Denote $s_{\min} = \min_z s(z)$. Then s_{\min} is the smallest span of the weld pool along the longitudinal direction (figure 10(b)). Figure 11 plots the smallest span versus the time after full penetration is established. It is apparent that the smallest span plays a critical role in completing the keyhole establishment process. That is, if the smallest span of

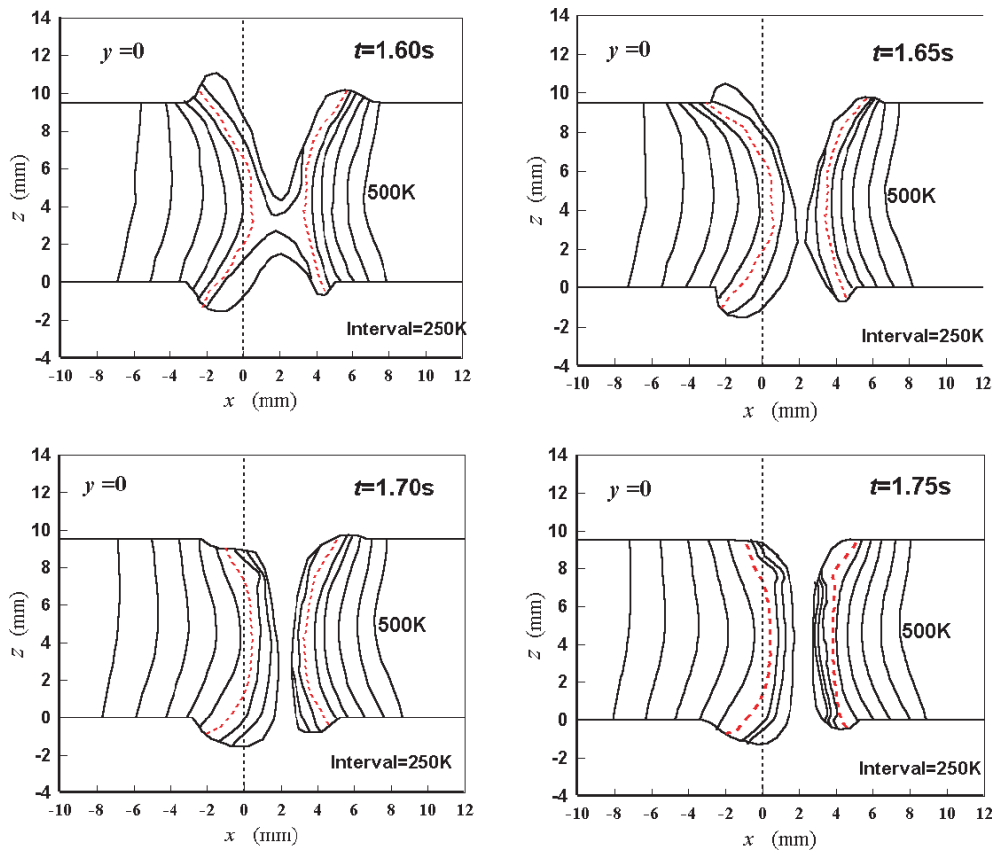


Figure 6. (Continued.)

the weld pool is not large enough, the conditions to complete keyhole establishment are not sufficient. The keyhole establishment process can only be completed after sufficient conditions are developed. It appears that the smallest span can give an appropriate measurement of the conditions sufficient to complete the keyhole establishment. After the conditions become sufficient, the keyhole establishment is completed at an extremely high speed, i.e. 40 mm s^{-1} depth increase rate. In the case analysed in this study, the conditions become sufficient at an approximate time of 1.5 s.

The formation of the cavities is caused by the arc pressure, which deforms the weld pool surface. In addition to the cavity, the overflow of the weld pool surface can also provide certain information about the welding process. In this study, the overflow is measured using the overflow height of the weld pool surface behind the arc as defined in figure 12. The development of the height for both sides of the weld pool surface can be obtained from figure 6. Figure 13 depicts the development of the heights for the two sides of the weld pool.

As can be seen in figure 13, the height of the GTAW pool quickly develops after the initial 0.5 s during which the mass of the melted metal accumulates from zero. It increases at a speed of 1.56 mm s^{-1} between $t = 0.5$ and 1 s. However, after this period, its growth becomes slow. The increase speed becomes approximately 0.48 mm s^{-1} . Such a slow increase process lasts until $t = 1.5$ s when the conditions for completing the keyhole establishment process become sufficient.

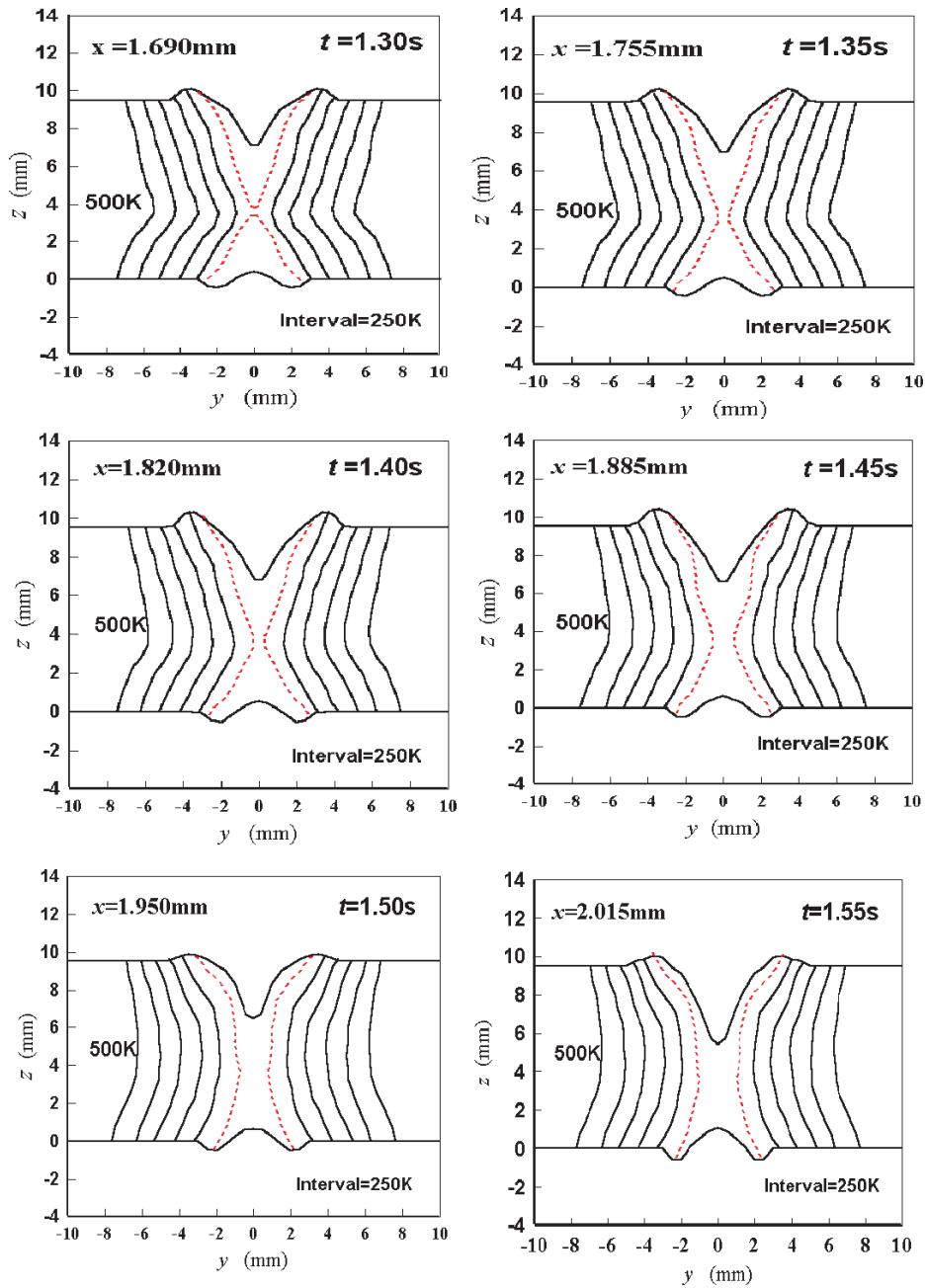


Figure 7. Dynamic development of transverse temperature field. The x -coordinate indicates the distance from the location where the arc was ignited. —, isothermal; ·····, liquid–solid boundary.

Figure 13 also shows that the height of the PAW pool increases at an approximately constant speed, 0.75 mm s^{-1} after the initial 0.5 s period of melted metal accumulation, until $t = 1.5 \text{ s}$. The average speed is smaller than that of the GTAW pool during the same period. Analysis of the process and the governing equations suggests that the gravitational force,

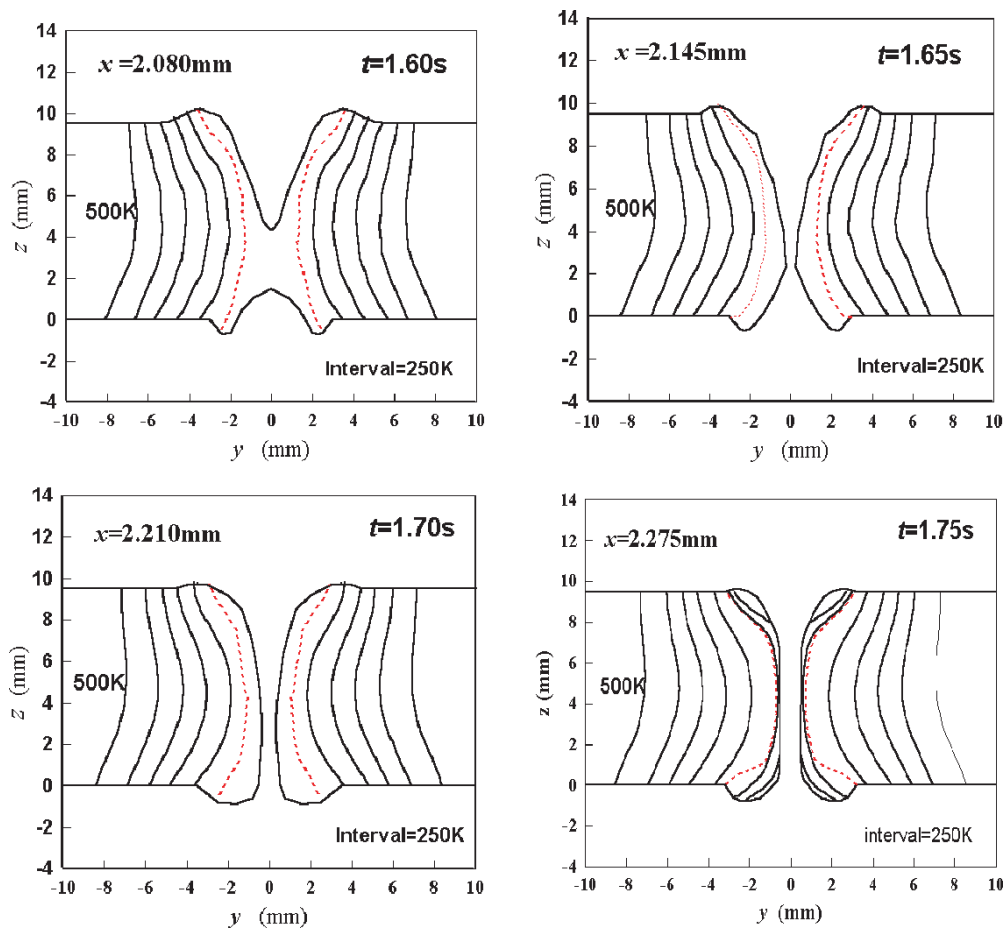


Figure 7. (Continued.)

and the gradient between the plasma arc pressure and the gas tungsten arc pressure after full penetration is established, are the primary causes. After the conditions for completing the keyhole establishment become sufficient at $t = 1.5$ s, the height quickly increases until the keyhole is fully established. After the keyhole is fully established, the overflow of the PAW pool diminishes at a high speed. At $t = 1.65$ s, the height is 1 mm. At $t = 1.7$ s, the overflow of the PAW pool completely diminishes. The diminishing speed is greater than 20 mm s^{-1} .

The developments of the depths of the weld pool on both the PAW and GTAW sides are plotted in figure 14. As can be observed in the figure, both the GTAW pool depth and PAW pool depth increase at approximately constant speed. As has been known, before full penetration is established, other geometrical parameters of the weld pool and the partial keyhole also change at approximately constant speeds. Hence, before full penetration is established, the DSAW process develops gradually. The dynamic keyhole establishment process may be divided into three periods: partial-penetration period, full-penetration period, and accelerated completion period. During the partial-penetration period, the process is in a stable growth state and all geometrical parameters of the weld pool and cavity or partial keyhole develop gradually. During the full-penetration period, the conditions for completing the keyhole establishment

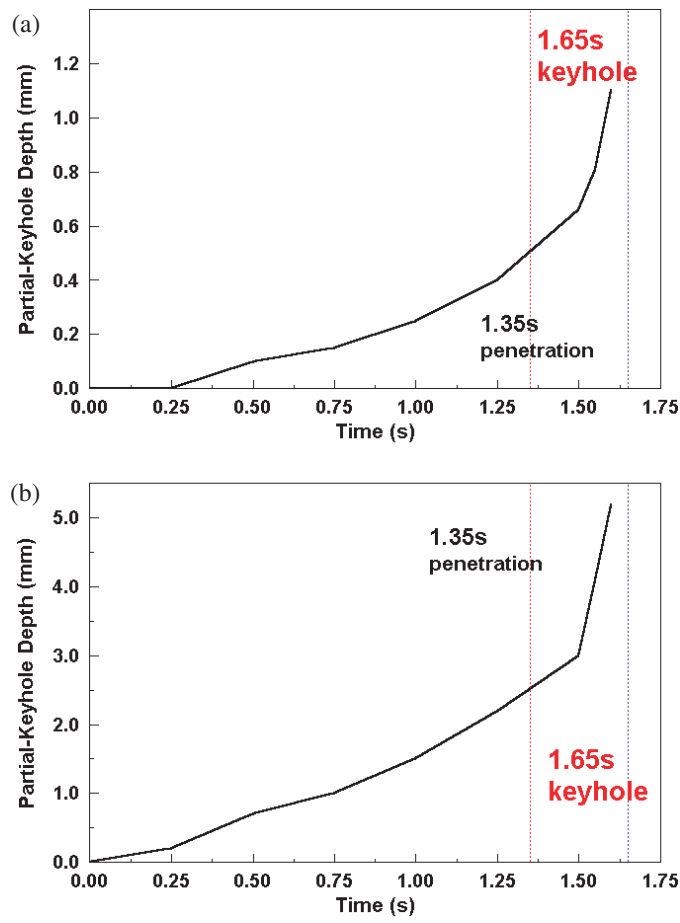


Figure 8. Development of cavity depth: (a) GTAW pool; (b) PAW pool.

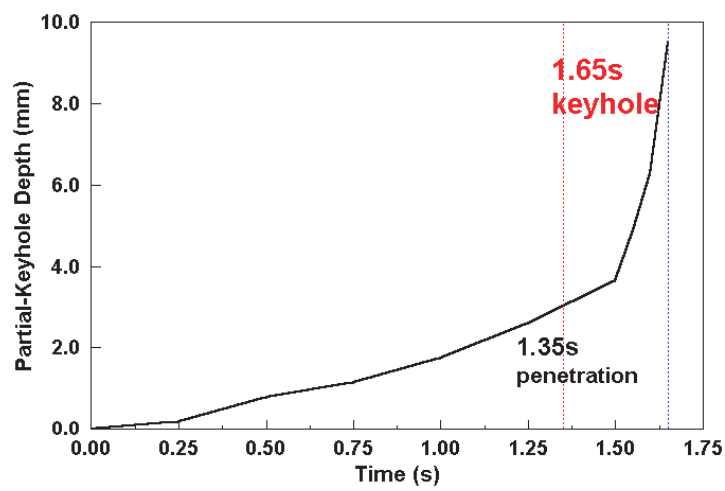


Figure 9. Development of depth of partial keyhole.

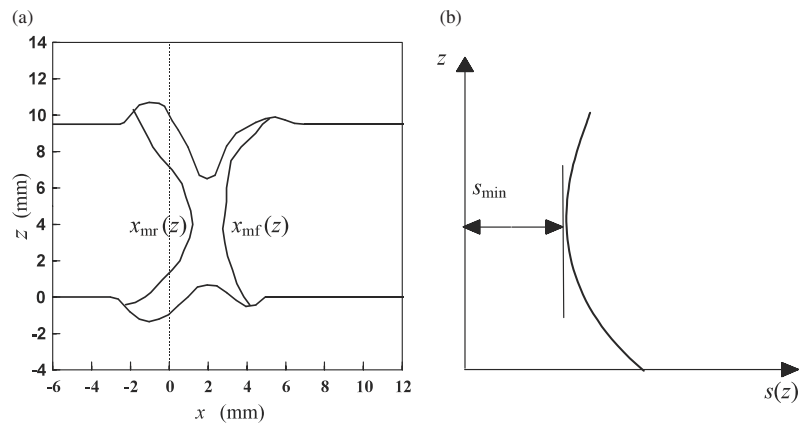


Figure 10. Definition of weld span: (a) weld front and rear profiles; (b) minimal span of weld.

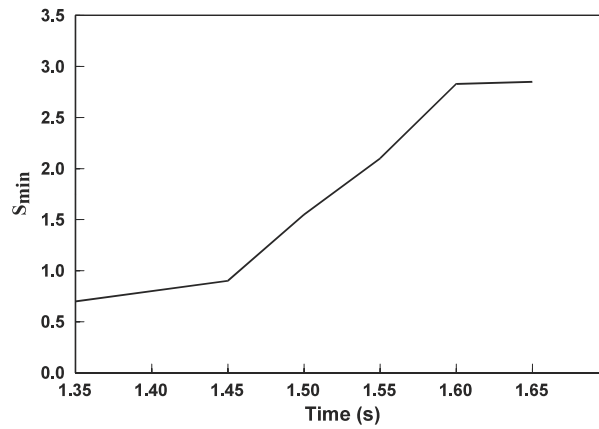


Figure 11. Development of minimal weld span.

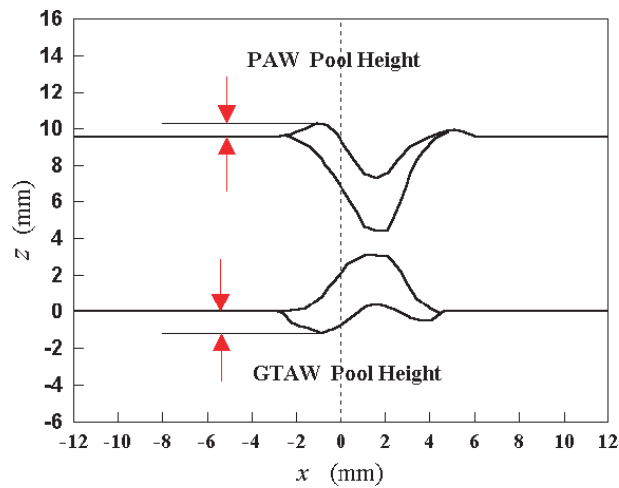


Figure 12. Definition of weld pool height.

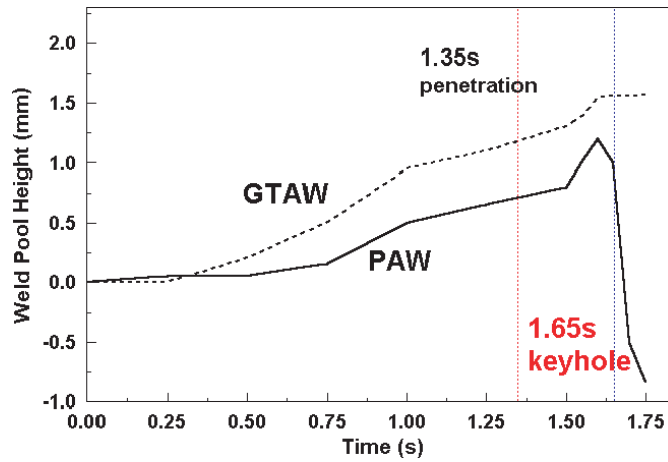


Figure 13. Development of weld pool height.

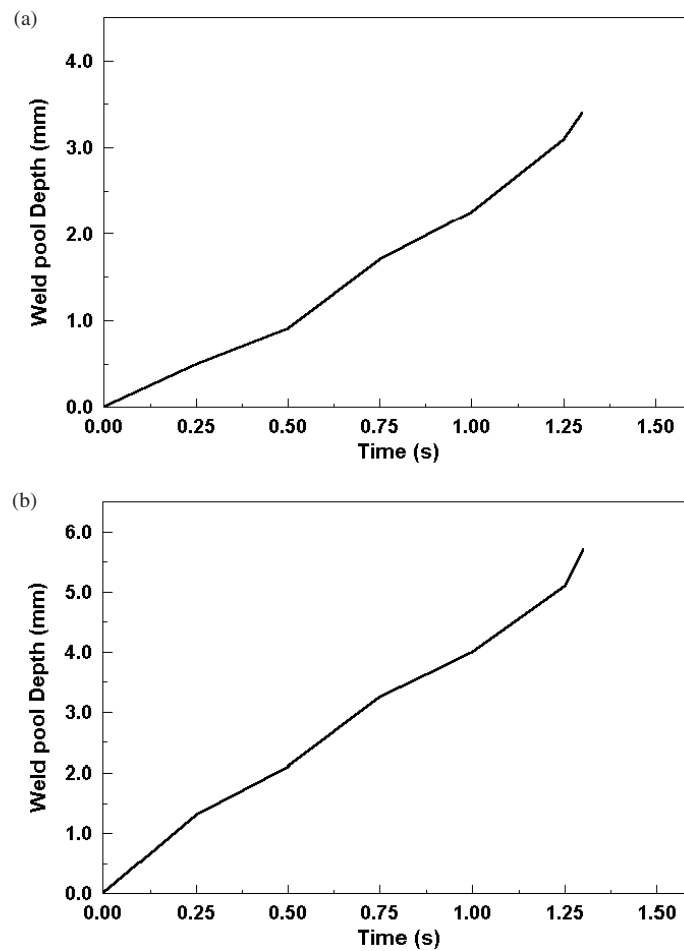


Figure 14. Development of weld pool depth: (a) GTAW pool depth; (b) PAW pool depth.

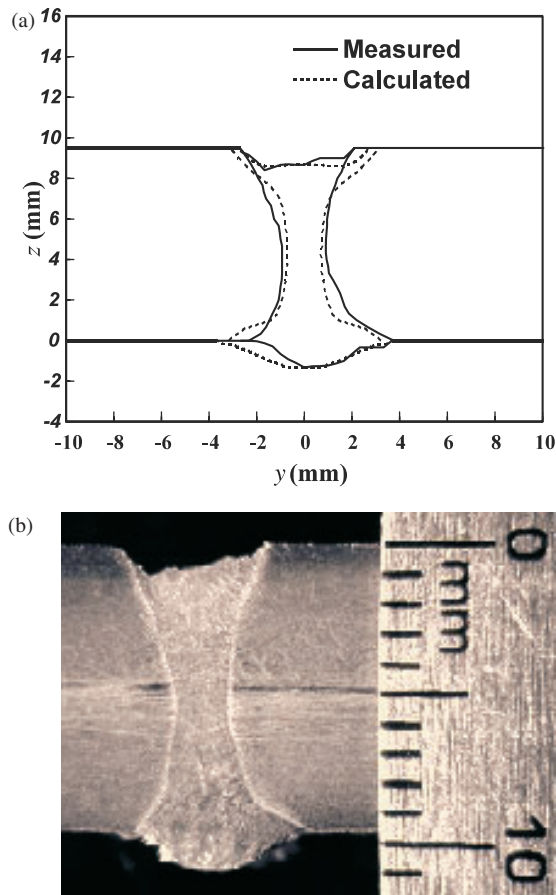


Figure 15. The comparison of measured and predicted keyhole double-sided arc butt weld on a 9.5 mm ($\frac{3}{8}$ inch) plate. Position, flat; welding current, 67 A; travel speed, 1.3 mm s^{-1} ; filler metal, none. (a) The measured and predicted DSAW weld geometry. (b) Macro-photography of DSAW weld.

are being established. When the conditions for completing the establishment of the keyhole become sufficient, the keyhole is quickly established during the accelerated completion period.

Figure 15 shows that the computed geometry of the weld zone agrees with the experimental result at a reasonable accuracy. The most pronounced characteristic of the DSAW process is its symmetric hour-glass-shaped weld, due to the symmetric double-sided and radial heating, as can be seen in figure 15. This unique characteristic, together with the deep narrow penetration capability, makes DSAW a promising competing process for joining larger metal structures. The numerical model developed is capable of predicting the fundamental characteristics of the DSAW process, such as the symmetrical hour-glass-shaped weld zone, and the deep narrow penetration capability.

It should be pointed out that this study and the developed numerical model will provide basic knowledge on the dynamic keyhole establishment which may be difficult to obtain experimentally. Such knowledge is fundamental for the further development of the DSAW process and its control. For example, to control the DSAW process, a reliable sensor is needed to detect the establishment of the keyhole. This study shows that detecting the height of the

PAW pool can be a possible method to detect the establishment of the keyhole because before the keyhole is fully established the height of the PAW pool increases while it decreases at a high speed after the establishment of the fully penetrated keyhole.

5. Conclusions

A numerical model has been developed to obtain data associated with the establishment process of the keyhole during DSAW. Analysis of the data revealed certain phenomena and dynamic behaviours associated with the DSAW process.

- (1) The establishment of the keyhole is completed primarily in a very short period at a very high speed. This period does not occur right after the workpiece is fully penetrated; instead, it occurs a period after the full penetration is developed. Analysis suggests that the smallest span, which starts to develop after the full penetration is established, of the weld pool along the longitudinal direction plays a critical role in determining the completion of the keyhole establishment.
- (2) The height of the overflow of the weld pool surface on the PAW side rapidly decreases after the keyhole is established. This phenomenon may provide the foundation needed to develop a keyhole sensor which is critical in the control of the DSAW process.
- (3) It is meaningful to divide the dynamic keyhole establishment process into three periods: partial-penetration period, full-penetration period, and accelerated completion period. During the partial-penetration period, the process is in a stable growth state and all geometrical parameters of the weld pool and cavity or partial keyhole develop gradually. During the full-penetration period, the conditions for completing the keyhole establishment are being established. When the conditions for completing the establishment of the keyhole become sufficient, the keyhole is quickly established during the accelerated completion period.

Acknowledgments

This work is supported by the National Science Foundation, USA under grant DMI-9812981 and the Ministry of Education Visiting Scholar Foundation of Key Laboratories in University, China.

References

- [1] Zhang Y M, Pan C X and Male A T 2000 Improvement of microstructures and properties of 6061 aluminum alloy weldments using double-sided arc welding process *Metall. Trans. A* **31** 2537–43
- [2] Zhang Y M, Zhang S B and Jiang M 2002 Keyhole double-sided arc welding process *Weld. J.* **81** 249s–55s
- [3] Zhang Y M, Zhang S B and Jiang M 2002 Sensing and control of double-sided arc welding process *ASME J. Manuf. Sci. Eng.* **124** 695–701
- [4] Mayott W 2000 A shipyard's preliminary assessment of double-sided arc welding process *Proc. How to Competitively Weld the 21st Century Ship Conf. (Norfolk, VA, 8–9 November 2000)* pp 277–89
- [5] Rokhlin S I and Guu A C 1993 A study of arc force, pool depression, and weld penetration during gas tungsten arc welding *Weld. J.* **72** 381s–90s
- [6] Oreper G M, Szekely J and Eagar T W 1986 Role of transient convection in the melting and solidification in arc weldpools *Metall. Trans. B* **17** 735–44
- [7] Oreper G M, Eagar T W and Szekely J 1983 Convection in arc weld pools *Weld. J.* **62** 307–12
- [8] Kou S and Sun D K 1985 Fluid flow and weld penetration in stationary arc welds *Metall. Trans. A* **16** 203–13
- [9] Lin M L and Eagar T W 1985 Influence of arc pressure on weld pool geometry *Weld. J.* **64** 163s–9s
- [10] Zacharia T, Eraslan A H and Aidun D K 1988 Modeling of non-autogenous welding *Weld. J.* **67** 18s–27s

- [11] Pardo E and Weckman D C 1989 Prediction of weld pool and reinforcement dimensions of GMA welds a finite-element model *Metall. Trans. B* **20** 937–47
- [12] Tekriwal P and Mazumder J 1988 Finite element analysis of three-dimensional transient heat transfer in GMA welding *Weld. J.* **67** 150s–6s
- [13] Sun J S and Wu C S 2001 Effects of welding heat input on microstructure and hardness in heat-affected zone of HQ130 steel *Modelling Simul. Mater. Sci. Eng.* **9** 25–36
- [14] Wu C S and Sun J S 1998 Determining the distribution of the heat content of filler metal droplets transferred into GMA weldpools *Proc. Inst. Mech. Eng. Part B: J. Eng. Manuf.* **B 212** 525–31
- [15] Keanini R G and Rubinsky B 1993 Three-dimensional simulation of the plasma arc welding process *Int. J. Heat Mass Transfer* **36** 3283–98
- [16] Dowden J and Kapadia P 1994 Plasma arc welding: a mathematical model of the arc *J. Phys. D: Appl. Phys.* **27** 902–10
- [17] Coletta V 1995 *College Physics* (Boston, MA: McGraw-Hill)
- [18] Bashenko V V and Sosnin N A 1998 Optimization of the plasma arc welding process *Weld. J.* **67** 233s–7s
- [19] Tsai N S and Eagar T W 1985 Distribution of the heat and current fluxes in gas tungsten *Metall. Trans. B* **16** 841–6
- [20] Wu C S and Dorn L 1995 Prediction of surface depression of a tungsten inert gas weld pool in the full-penetrated condition. *Proc. Inst. Mech. Eng. Part B: J. Eng. Manuf.* **209** 221–6
- [21] Wu C S and Dorn L 1994 Computer simulation of fluid dynamics and heat transfer in full-penetrated TIG weld pools with surface depression *Comput. Mater. Sci.* **2** 341–9
- [22] Wu C S 1992 Computer simulation of three-dimensional convection in travelling MIG weld pools *Eng. Comput.* **9** 529–37
- [23] Pehlke R D Summary of thermal properties for casting alloys and mold materials, Department of Materials and Metallurgical Engineering, University of Michigan, Ann Arbor, Michigan
- [24] Baucchio M (ed) 1993 *ASM Metals Reference Book* 3rd edn (Materials Park, OH: ASM International) p 361
- [25] Lancaster J F 1986 *The Physics of Welding* (Oxford: Pergamon Press) p 28